Hybrid Ni$_2$P/CoP Nanosheets as Efficient and Robust Electrocatalysts for Domestic Wastewater Splitting

Yeshu Tan[1], Jianrui Feng[1], Liqun Kang[2], Longxiang Liu[1], Fangjia Zhao[1], Siyu Zhao[1], Dan J.L. Brett[3], Paul R. Shearing[3], Guanjie He[1.3.4]* and Ivan P. Parkin[1]*

[1]*Christopher Ingold Laboratory, Department of Chemistry, University College London, 20 Gordon Street, London WC1H 0AJ, United Kingdom. Email: g.he@ucl.ac.uk; i.p.parkin@ucl.ac.uk*

[2]*Materials and Catalysis Laboratory, Department of Chemical Engineering, University College London, London WC1E 7JE, United Kingdom.*

[3]*Electrochemical Innovation Laboratory, Department of Chemical Engineering, University College London, London WC1E 7JE, United Kingdom.*

[4]*School of Chemistry, University of Lincoln, Joseph Banks Laboratories, Green Lane, Lincoln, LN6 7DL, United Kingdom.*

Abstract

The development of low-cost, robust and efficient non-noble metal electrocatalysts is still a pursuit for the hydrogen evolution reaction (HER). Herein, a self-standing electrocatalyst, Ni_2P/CoP nanosheet, was fabricated directly on three-dimensional Ni foams by two facile steps, which illustrated both high activity and stability for HER in different electrolytes. Benefiting from the porous structures of nanosheets with large specific surface area and the hybrid Ni_2P/CoP, the as-prepared electrocatalyst presented remarkable HER with overpotentials of 65.2 mV and 87.8 mV to reach a current density of -10 mA cm^{-2} in neutral and alkaline media, respectively. Density function theory calculations revealed a lower activation energy of water dissociation and efficient HER steps of hybrid Ni_2P/CoP nanosheets compared with mono CoP. The self-standing electrocatalyst maintained excellent chemical stability. Additionally, the HER process in domestic wastewater was realized with more impressive performance by using Ni_2P/CoP nanosheets compared with commercial Pt/C. Hydrogen was continuously generated for 20 h in mildly alkaline dishwashing wastewater. This work provides a feasible way to fabricate non-noble metal and self-standing hybrid bimetallic phosphides for HER in neutral and alkaline media, showing great potential for efficient hydrogen production by re-utilizing wastewater resources.

Keywords: Hybrid; Ni_2P/CoP nanosheet; Self-standing; Hydrogen evolution reaction; Wastewater splitting

1. Introduction

With increasing energy demands and the rising development of clean energy technologies, hydrogen has been regarded as one of the most promising alternatives to fossil fuels due to its high energy density (142 MJ kg^{-1}) and environmental-friendly properties.[1-4] Water electrolysis is an industrially applicable strategy to generate hydrogen.[5-8] The process consists of two half-reactions, which are the hydrogen evolution reaction (HER) and the oxygen evolution reaction (OER).[9-11] Both reactions are crucial for the overall efficiency. The state-of-the-art electrocatalysts for HER are platinum-based materials.[12-16] However, the high cost and scarcity of platinum sources restrict their wide applications. Therefore, non-noble metal and efficient electrocatalysts, such as Ni_5P_4,[17] $NiFeO_x$,[18] MoO_2[19] and $NiMoCo$[20] for HER, have been developed.[21-23] Among these materials, self-standing electrocatalysts have been considered as efficient electrodes to avoid the dispersion and dissolution problem and simplify the fabrication process.[24-25] Additionally, efficient HER electrocatalysts in neutral and alkaline media have been developed in recent years, which widen the working condition of HER in more practical electrolytes, such as towards using domestic and industrial wastewater.[26-28] The application of HER electrocatalysts to split wastewater paves a new way to recycle energy, which is currently less explored.

To date, transition metal phosphides (TMPs) like CoP,[29] Ni_2P[30] and Ni_5P_4[31] have been developed as efficient HER electrocatalysts because of their inherent advantages over oxides or hydroxides.[32-35] Phosphorus can not only moderate interactions with catalytic intermediates, but also act as an anchor to bind with protons.[36] Moreover, the

proper combination of metal and phosphorus exhibits very high electrical conductivity.[37-38] Bimetallic phosphides including CoP/MoP,[39] FeP/Ni$_2$P,[40] FeCoP[41] and Ni$_2$P/Cu$_3$P[42] show superior HER performances.[43-44] Introducing an additional metal into TMP can further increase the HER performance due to the tuning of electronic structures and synergistic effects. In recent work, Ni$_2$P/Cu$_3$P were fabricated through the *in-situ* growth method on NiCuC foils, the overpotential at the current density of -10 mA cm^{-2} of modified Ni$_2$P/Cu$_3$P and mono Ni$_2$P were 78 mV and 199 mV, indicating the efficient synergistic effect of bimetallic phosphides for HER.[42] Moreover, Ren's group reported a bimetallic phosphide (FeP/Ni$_2$P) electrocatalyst, showing both superior HER and OER performances. DFT calculations revealed the successful tuning of hydrogen adsorption energy and exposure of active facets, which were different from typical FeP crystals.[45] In electrocatalysts, surface morphology plays a key role in water electrolysis. Nanowires, nanoflowers and nanotubes were developed showing increased HER performances because of their large specific surface area and efficient active sites.[45-46] However, current synthetic strategies for bimetallic phosphides with rough and uniform surfaces are relatively complicated.

Herein, a facile synthetic method is presented to fabricate hybrid Ni$_2$P/CoP nanosheets based on Ni support foams. The robust Ni$_2$P/CoP nanosheets show remarkable and stable HER performances in both neutral and alkaline media. DFT calculation reveals lower activation energy for water dissociation and more efficient associative desorption of hydrogen for bimetallic phosphides, which are crucial for HER in neutral and alkaline media. The as-prepared electrocatalyst also delivers an

outstanding HER performance in alkaline domestic wastewater with an overpotential of 315 mV to reach a current density of -10 mA cm^{-2} and a stable hydrogen generation for over 20 h, which is superior to commercial Pt/C catalysts. The developed electrocatalysts show excellent HER performance in different media, and have great potential for practical applications to generate renewable energy from domestic wastewater.

2. Results and Discussion

2.1. Synthesis and structure characterization

The fabrication procedure of Ni$_2$P/CoP nanosheets followed a facile two-step strategy, as shown in **Figure 1**. First, commercial Ni foam is used as the substrate, nickel hydroxide and cobalt hydroxide layered nanosheet arrays were fabricated through the electrodeposition in a three-electrode cell with cobalt nitrate solution as the electrolyte. Pt foil, Ag/AgCl and Ni foam are used as the counter, reference and working electrodes, respectively. The X-ray diffraction (XRD) pattern (**Figure S1**) illustrates the phase information of Ni foam-Ni(OH)$_2$/Co(OH)$_2$ precursors. Scanning electron microscope (SEM) images (**Figure S2**) show the original Ni foam surface and layered nanosheet morphology after the electrodeposition. The Ni foam has a porous structure and its surface is flat, after the electrodeposition, layered nanosheets are formed. Then, the as-prepared precursor is transferred into a tube furnace for a phosphating process at 350 $^{\circ}$C for 1 h. The phosphating process is ascribed to the PH$_3$ flow, which is released by the decomposition of NaH$_2$PO$_2$. The Ni$_2$P/CoP electrocatalysts with different electrodeposition times were fabricated through the same two-step method.
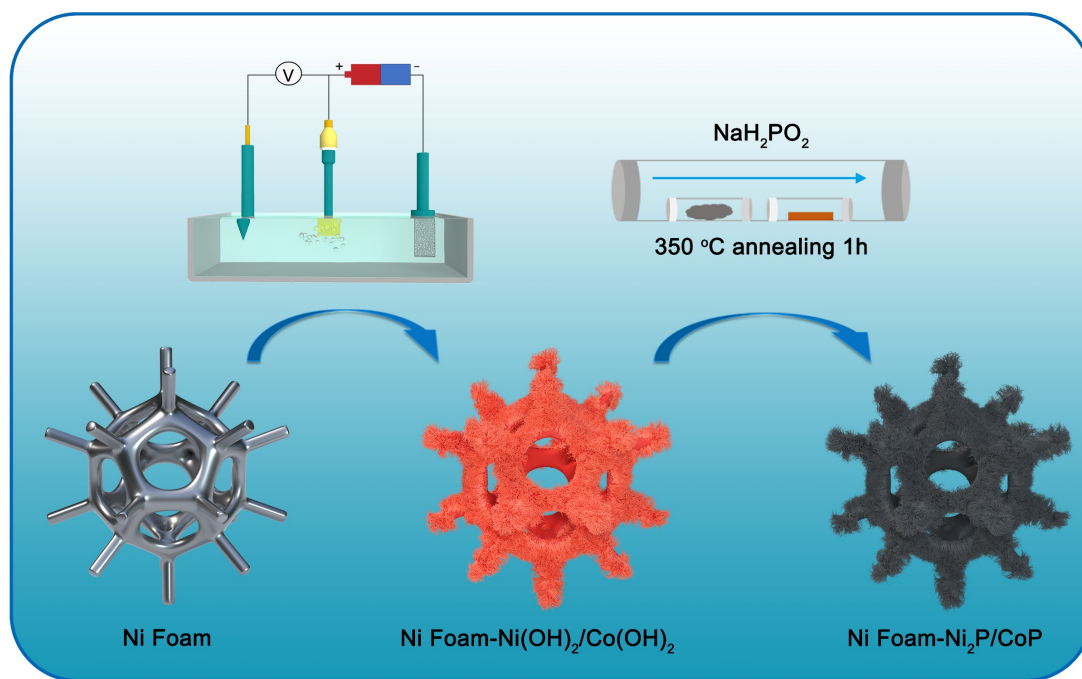
Figure 1. Graphic display of the fabrication of hybrid Ni$_2$P/CoP nanosheets directly on Ni foams.

The XRD patterns in **Figure S3** indicate the coexistence of Ni$_2$P and CoP crystal structures on the Ni foam. The morphology of as-prepared materials is uniform and remains as layered nanosheets, as shown in **Figure 2a,** characterized by SEM. The shape of nanosheets ensures more efficient exposure of active sites and rapid release of hydrogen bubbles. The transmission electron microscopy (TEM) image shown in **Figure 2b** reveals more detailed morphology information, the nanosheets are thin and cross-linked. The lattice spaces of 2.54 Å and 2.23 Å represent (200) lattice planes of CoP and (111) of Ni$_2$P, respectively, as shown from the high-resolution TEM (HRTEM) image in **Figure 2c**. The inverse fast Fourier transform (FFT) filtered HRTEM images of lattice fringes and distance diagram are provided in **Figure 2d**. The distance diagram shows clear lattice spaces of CoP (200) and Ni$_2$P (111). The insets show the inverse FFT filtered HRTEM images on the selected area. The selected area electron diffraction

pattern (SAED) was shown in **Figure S4**. Additionally, the bright-field scanning transmission electron microscopy (BF-STEM) image and its energy-dispersive spectroscopy (EDS) mapping images are shown in **Figure 2e**, illustrating the homogeneous dispersion of Ni, Co, P and O species. The estimated atomic ratio of Ni, Co, P and O obtained from EDS spectra is approximately 3:7:10:11, as shown in **Figure S5**. The ratio between CoP and Ni_2P is 14:3, indicating that CoP is the domination in the hybrid electrocatalyst.
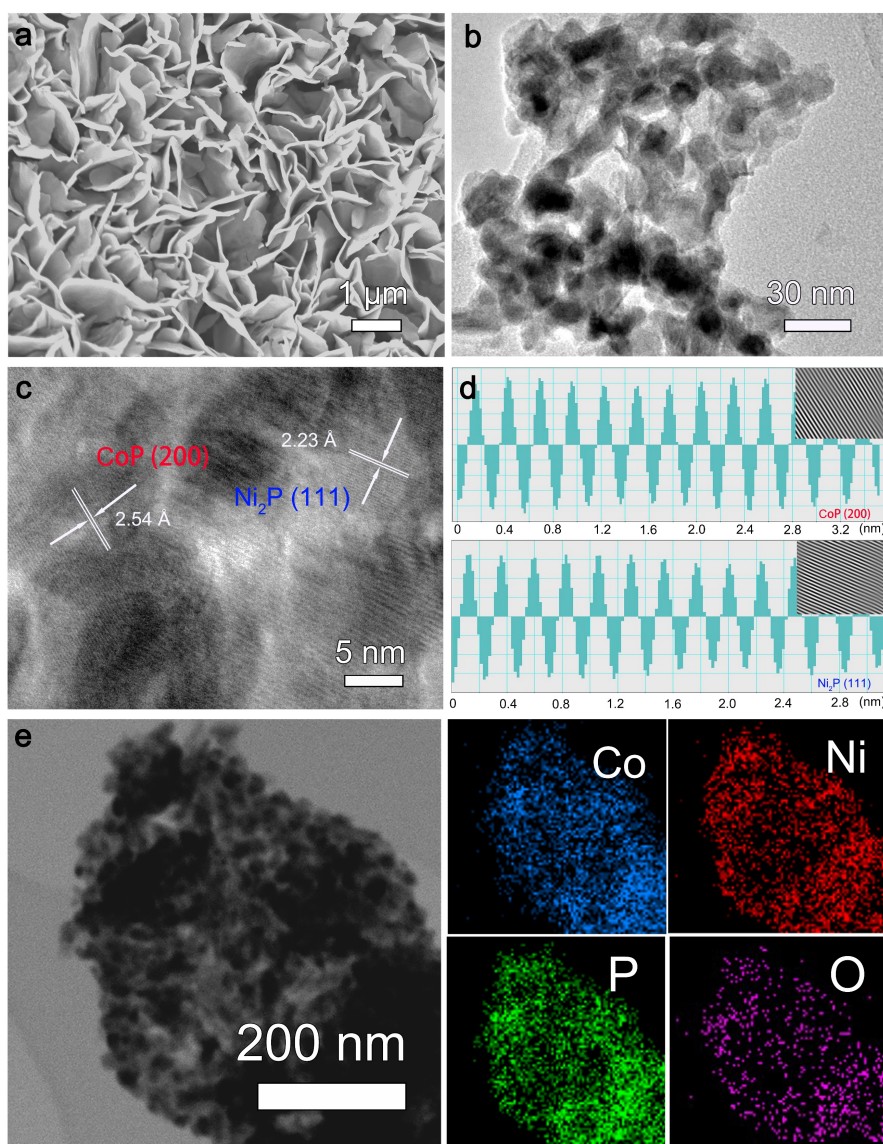

Figure 2. Morphology of Ni_2P/CoP. (a) SEM images, (b) TEM image, (c) HRTEM image, (d) Lattice distance diagram and inverse FFT filtered HRTEM image (inset). (e)

BF-STEM and corresponding EDS elemental mapping images of Ni_2P/CoP.

X-ray photoelectron spectroscopy (XPS) was used to determine valence states and the composition information of hybrid Ni_2P/CoP. The elements of Ni, Co, P, C and O can be clearly illustrated in **Figure S6**. The peak after the deconvolution located at 853.6 eV is assigned to metallic Ni in **Figure S7**. Moreover, the other two peaks located at 857.4 eV and 874.9 eV correspond to Ni^{2+}.[47] The additional peaks at 862.8 eV and 880.5 eV can be assigned to the satellite peak. **Figure S8** presents the XPS spectra of Co 2p, after the deconvolution, the peaks at 777.8 eV and 781.2 eV are fitted to Co $2p_{3/2}$, while the peaks at 792.9 eV and 797.6 eV are ascribed to Co $2p_{1/2}$, the other two peaks of 803.4 eV and 786.1 eV are satellite peaks.[48] As shown in **Figure S9**, the peaks at 133.2 eV, 130.0 eV and 129.1 eV are assigned for oxidized metal phosphates, P $2p_{1/2}$ and P $2p_{3/2}$, respectively. The oxidized metal phosphate peak is due to exposure to air.[49]

To better understand the electronic structure of Ni and Co, as well as identify the surface O species, an *ex-situ* near edge X-ray absorption file structure (NEXAFS) study was carried out at Ni L-edge, Co L-edge and O K-edge, respectively, as shown in **Figure 3**. Ni L_3-edge NEXAFS probes the dipole-allowed electron transitions from Ni $2p_{3/2}$ to unoccupied 3d orbitals, in which the two main absorption features at 853.0 and 855.0 eV match quite well with that of NiO and $Ni(OH)_2$ standards, as shown in **Figure 3a**, suggesting a Ni^{2+} dominant composition. Similarly, Co L-edge NEXAFS spectra of Ni_2P/CoP, CoP, Co_3O_4 and CoO are compared in **Figure 3b** to investigate the valence states and geometry of Co species in the catalysts. Spectra of both Ni_2P/CoP and CoP consists of a multiple L_3-edge peak split by four sub-peaks at 777.5, 778.7, 779.3 and

780.0 V, respectively. There is also an additional charge-transfer shoulder peak at 782.2 eV. These multiple peaks are in good agreement with the absorption features in NEXAFS spectra of CoO standard, in which only high spin Co^{2+} are present in octahedral geometry (O_h).[50-51] In addition, these peak features also corresponds well to $Co_3(PO_4)_2$[52-53] and $Co(OH)_2$.[54] O K-edge NEXAFS characterization directly probes the chemical states of the surface oxygen species. In **Figure 3c**, two absorption features at 533.0 and 537.5 eV are found in CoP and Ni_2P/CoP samples. Such peaks are not observed in Co_3O_4, $Ni(OH)_2$ or NiO,[55-57] but are very similar to phosphate,[53] which is phosphide oxide due to the exposure to air. The surface oxidation species have limited influence on HER performance. The fresh samples were used for HER test immediately, which means less surface oxides. During HER process, negative potential was applied on the working electrode, which will lead to the reduction of Co-O species and dissolution of oxidized P species in neutral or alkaline media as reported in research work.[58-59] Thus, the small amount of surface oxides species will disappear after continuous HER process. The XPS results, NEXAFS analysis, morphology and crystal characterization confirm the successful fabrication of bimetallic transition metal phosphides, Ni_2P/CoP nanosheets.

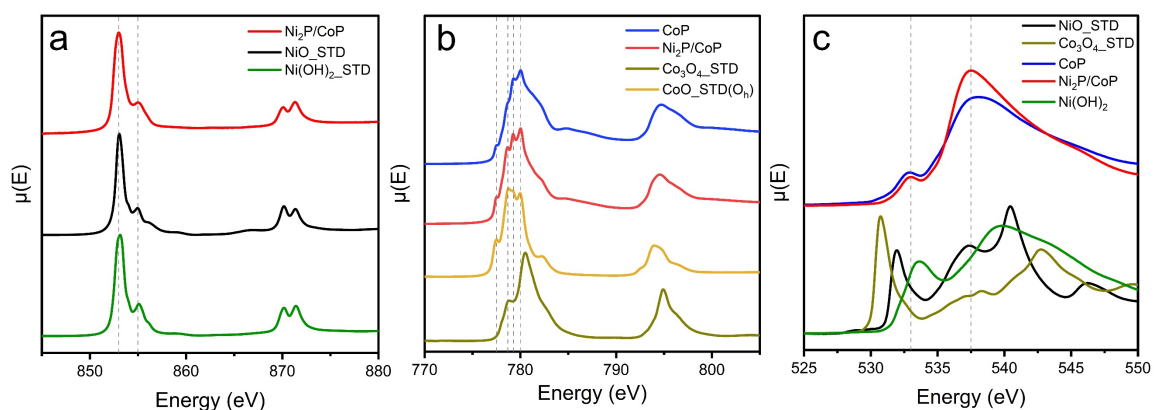Figure 3. NEXAFS spectra of (a) Ni $L_{3,2}$-edge of Ni_2P/CoP, NiO and $Ni(OH)_2$ standards, (b) Co $L_{3,2}$-edge of Ni_2P/CoP, CoP, Co_3O_4 and CoO standards, (c) O K-edge of CoP, Ni_2P/CoP, Co_3O_4, $Ni(OH)_2$ and NiO standards.

2.2. Electrocatalytic performance

The electrocatalytic performance of electrocatalysts prepared from different electrodeposition times for HER was evaluated in both neutral and alkaline media. To better understand the advantages of hybrid Ni_2P/CoP, CoP and Ni_2P were synthesized through the same two-step method on carbon paper, which is discussed in the experimental section. The XRD pattern illustrated in **Figure S10** confirmed the successful synthesis of CoP and Ni_2P; moreover, there was a very small amount of Co_2P or NiP. The morphologies of CoP and Ni_2P are different from hybrid Ni_2P/CoP, as shown in **Figure S11**. The SEM image illustrates that the shape of CoP is similar to nano-pellets, while the shape of Ni_2P was irregular in the SEM image.
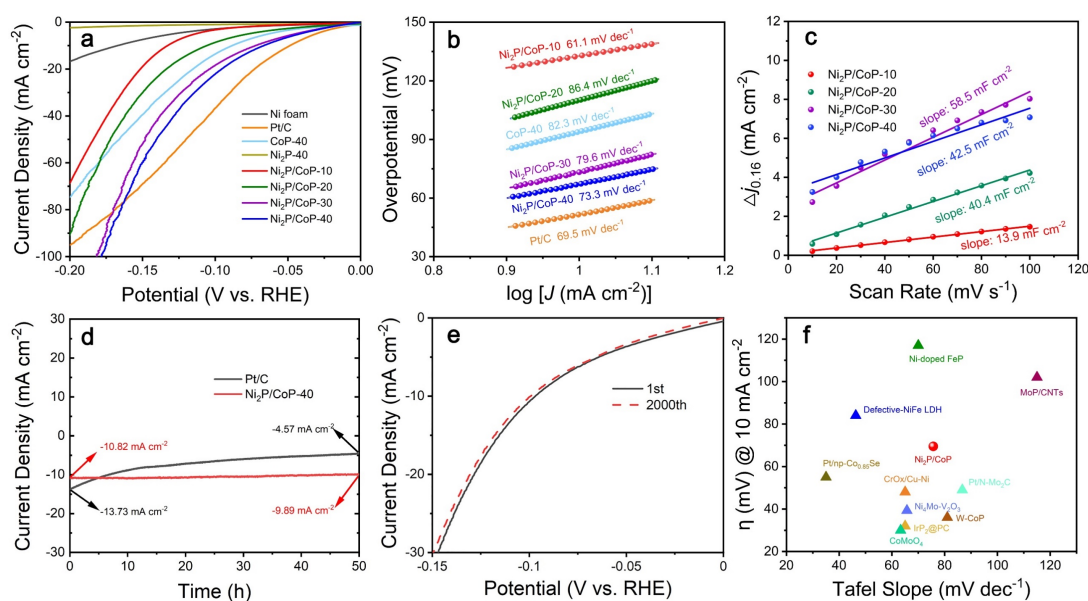

Figure 4. HER performance in 1M PBS. (a) HER performance of Ni_2P/CoP with different deposition times, CoP, Ni_2P and commercial Pt/C in 1M PBS. (b) Tafel plots

and (c) double-layer capacitances (C_{dl}) of Ni$_2$P/CoP with different electrodeposition times. (d) Chronoamperometry test and (e) 2000 cycles of LSV curves of Ni$_2$P/CoP-40 performed in 1M PBS. (f) Comparison of the state-of-the-art catalysts as for both Tafel slopes and overpotentials (η_{10}), with references in neutral media.

The as-prepared hybrid Ni$_2$P/CoP electrocatalysts show superior electrocatalytic performance in 1 M phosphate buffer saline (PBS) solution. The HER performance of Ni foam, commercial Pt/C, CoP-40, Ni$_2$P-40, Ni$_2$P/CoP-10, Ni$_2$P/CoP-20, Ni$_2$P/CoP-30 and Ni$_2$P/CoP-40 are shown in **Figure 4a** (the label behind the catalysts represents the electrodeposition time (mins) in the first synthetic step). The loading of Pt is 1 mg cm^{-2} in the as-prepared Pt/C electrode. At the current density of -10 mA cm^{-2}, the overpotentials (η_{10}) are 170 mV, 50.1 mV, 94.1 mV, 385 mV, 133 mV, 109 mV, 73.4 mV and 65.2 mV, respectively. The HER performance of hybrid Ni$_2$P/CoP raised with the increase of the deposition time. It is worth to note that CoP-40 shows limited performance compared with Ni$_2$P/CoP-40, confirming the synergetic effect between CoP and Ni$_2$P, facilitating the HER process. Introducing an additional transition metal into TMP will tune the electronic properties. The non-noble Ni$_2$P/CoP-40 nanosheets exhibit comparable HER performance in 1M PBS with commercial Pt/C catalysts. The longer electrodeposition times after 30 mins do not contribute to the rapid performance increase, attributing to the realization of maximum active sites on the surface with saturated Ni$_2$P/CoP. The corresponding Tafel slopes in **Figure 4b** of commercial Pt/C, CoP-40, Ni$_2$P/CoP-10, Ni$_2$P/CoP-20, Ni$_2$P/CoP-30 and Ni$_2$P/CoP-40 are 69.5 mV dec^{-1}, 82.3 mV dec^{-1}, 61.1 mV dec^{-1}, 86.4 mV dec^{-1}, 79.6 mV dec^{-1} and 73.3 mV dec^{-1},

respectively, confirming the rate-limiting step of Volmer-Heyrovsky step for HER in neutral media. The Ni$_2$P/CoP-30 and the Ni$_2$P/CoP-40 show similar performances, which may be ascribed to the overlap of active sites on the surface with an increasing amount of Ni$_2$P and CoP. To better understand the effect of electrodeposition time, electrochemically active surface area (ECSA) was investigated using cyclic voltammetry (CV), as shown in **Figure S12**. With the increase of the electrodeposition time, the double-layer capacitance increased first, and then decreased, indicating the effective electrodeposition time, as shown in **Figure 4c**. The double-layer capacitance (C_{dl}) of Ni$_2$P/CoP-10, Ni$_2$P/CoP-20, Ni$_2$P/CoP-30 and Ni$_2$P/CoP-40 are 13.9 mF cm^{-2}, 40.4 mF cm^{-2}, 58.5 mF cm^{-2} and 42.5 mF cm^{-2}, respectively. Ni$_2$P/CoP-30 has the highest number of active sites, indicating the most suitable electrodeposition time. If the electrodeposition time is less than 30 mins, the performance will further increase. Ni$_2$P/CoP-40 has the lowest overpotential, but its C_{dl} starts to decrease, so the electrodeposition time beyond 40 mins is not suggested. Electrochemical impedance spectroscopy (EIS) curves are shown in **Figure S13**. Inset shows the electrical equivalent circuit. R$_{ct}$ represents charge transfer resistance, R$_s$ is related to solution resistance and CPE is attributed to the double-layer capacitance. The R$_{ct}$ was extracted from the simulated circuit. In 1M PBS media, the R$_{ct}$ of Ni$_2$P-40, CoP-40 and Ni$_2$P/CoP-40 were 6.54 ohm, 4.53 ohm and 3.19 ohm. The hybrid Ni$_2$P/CoP electrocatalyst had the smallest R$_{ct}$, indicating the fast charge transfer during the HER process. The commercial Pt/C shows the lowest overpotential at η_{10}, but Ni$_2$P/CoP-40 has the lowest overpotential at η_{100}, presenting the efficient performance with increasing applied

potential. The durability evaluations are shown in **Figure 4d**. A constant potential of -0.78 V *vs* Ag/AgCl was applied on Ni_2P/CoP-40 electrocatalyst, which has an initial current density of -10.82 mA cm^{-2}, the current density increases at first during the activation process and then decreases to -9.89 mA cm^{-2} after 50 h in 1M PBS, illustrating the remarkable durability while the commercial Pt/C shows fragile stability. The current density of Pt/C decreases from -13.73 mA cm^{-2} to -4.57 mA cm^{-2} within the same period. Meantime, the neglectable decrease of Ni_2P/CoP-40 after 2000 continuous linear sweep voltammetry (LSV) cycles further confirms its excellent stability as shown in **Figure 4e**. The corresponding Pt/C stability is shown in **Figure S14**. The Pt/C electrocatalysts faced the instability during long-term reaction, which highlights the advantage of self-standing electrocatalysts. The SEM and HRTEM image after 50 h test indicate the structure stability of Ni_2P/CoP-40, as shown in **Figure S15**. The nanosheets showed the vertical morphology and shapes had no significant change, as shown by thin nanosheets in the TEM image, confirming its structural stability. Among the recent electrocatalysts for HER in 1M PBS, hybrid Ni_2P/CoP shows comparable or even better HER performances based on the overpotential (η_{10}) and Tafel slope, as shown in **Figure 4f**. Detailed information is listed in **Supplemental Table 1**.
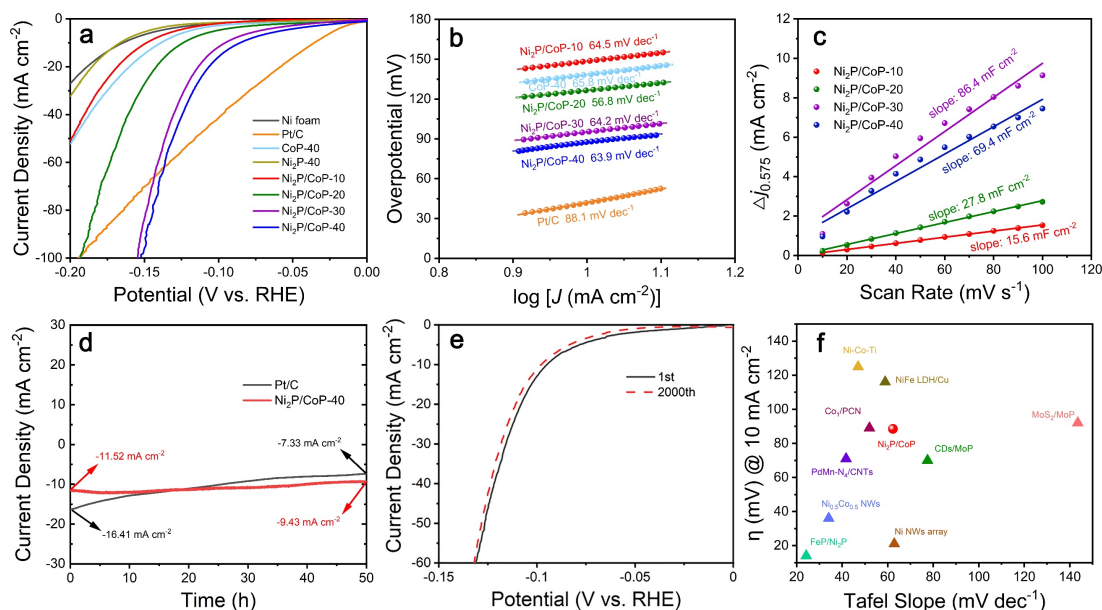
Figure 5. HER performance in 1M KOH. (a) HER performance of Ni_2P/CoP with different deposition times, CoP, Ni_2P and commercial Pt/C in 1M KOH. (b) Tafel plots and (c) double-layer capacitances (C_{dl}) of Ni_2P/CoP with different electrodeposition times. (d) Chronoamperometry test and (e) 2000 cycles of LSV curves of Ni_2P/CoP-40 performed in 1M KOH. (f) Comparison of the state-of-the-art catalysts as for both Tafel slopes and overpotentials (η_{10}), with references in alkaline media.

Additionally, the HER electrocatalytic performances of the Ni foam, commercial Pt/C, CoP, Ni_2P/CoP are examined in 1 M KOH, as shown in **Figure 5a**. At a geometric current density of -10 mA cm^{-2}, the overpotential (η_{10}) of original Ni foams, commercial Pt/C, CoP-40, Ni_2P-40, Ni_2P/CoP-10, Ni_2P/CoP-20, Ni_2P/CoP-30 and Ni_2P/CoP-40 are 164 mV, 38.5 mV, 140 mV, 178 mV, 149 mV, 127 mV, 96.1 mV and 87.8 mV, respectively. The increasing trend of HER performance in alkaline media for hybrid Ni_2P/CoP is consistent with that in neutral media. The CoP-40 alone shows limited performance, which is similar to Ni_2P/CoP-10, further confirming the successful introduction of Ni_2P into CoP. The Tafel slope of commercial Pt/C, CoP-40, Ni_2P/CoP-

10, Ni$_2$P/CoP-20, Ni$_2$P/CoP-30 and Ni$_2$P/CoP-40 are 88.1 mV dec^{-1}, 65.8 mV dec^{-1}, 64.5 mV dec^{-1}, 56.8 mV dec^{-1}, 64.2 mV dec^{-1} and 63.9 mV dec^{-1}, as shown in **Figure 5b.** Tafel slopes of as-prepared electrocatalysts indicate that the Volmer-Heyrovsky mechanism is the rate-determining. The overpotential (η_{100}) at the current density of - 100 mA cm^{-2} for Pt/C and Ni$_2$P/CoP-40 are 197 mV and 151 mV, presenting faster reaction kinetics for Ni$_2$P/CoP-40 in the high current density range. The CV curves and ECSA analysis are evaluated in **Figure S16**. The double-layer capacitance (C$_{dl}$) of Ni$_2$P/CoP-10, Ni$_2$P/CoP-20, Ni$_2$P/CoP-30 and Ni$_2$P/CoP-40 are 15.6 mF cm^{-2}, 27.8 mF cm^{-2}, 86.4 mF cm^{-2} and 69.4 mF cm^{-2}, respectively, as shown in **Figure 5c**. The results are consistent with those discussed in neutral media. The EIS curves and electrical equivalent circuit are shown in **Figure S17**. The R$_{ct}$ of Ni$_2$P-40, CoP-40 and Ni$_2$P/CoP-40 were 8.38 ohm, 3.16 ohm and 0.82 ohm in 1M KOH, respectively, indicating the same trend of faster charge transfer of Ni$_2$P/CoP. The durability test was evaluated at a constant potential of -1.12 V *vs.* Ag/AgCl on Ni$_2$P/CoP-40 for 50 hours as shown in **Figure 5d**. The current density of the Ni$_2$P/CoP-40 electrocatalyst only decreases from -11.52 mA cm^{-2} to -9.43 mA cm^{-2}, showing its remarkable stability, while the current density of commercial Pt/C catalyst decreases from -16.41 mA cm^{-2} to -7.33 mA cm^{-2} after 50 hours. **Figure 5e** shows the LSV curves of Ni$_2$P/CoP-40 after 2000 cycles in 1M KOH, the performance shows a negligible decrease, further illustrating its robust performance. The commercial Pt/C catalyst shows a large decrease after 2000 cycles in 1M KOH, as shown in **Figure S18**. The as-prepared electrocatalysts show comparable or even better performance based on the overpotential (η_{10}) and the Tafel slope

compared to recent state-of-the-art studies as shown in **Figure 5f**. Detailed information

is listed in **Supplemental Table 2** in the supporting information. The hybrid Ni_2P/CoP

nanosheets show remarkable HER performance both in neutral and alkaline media.
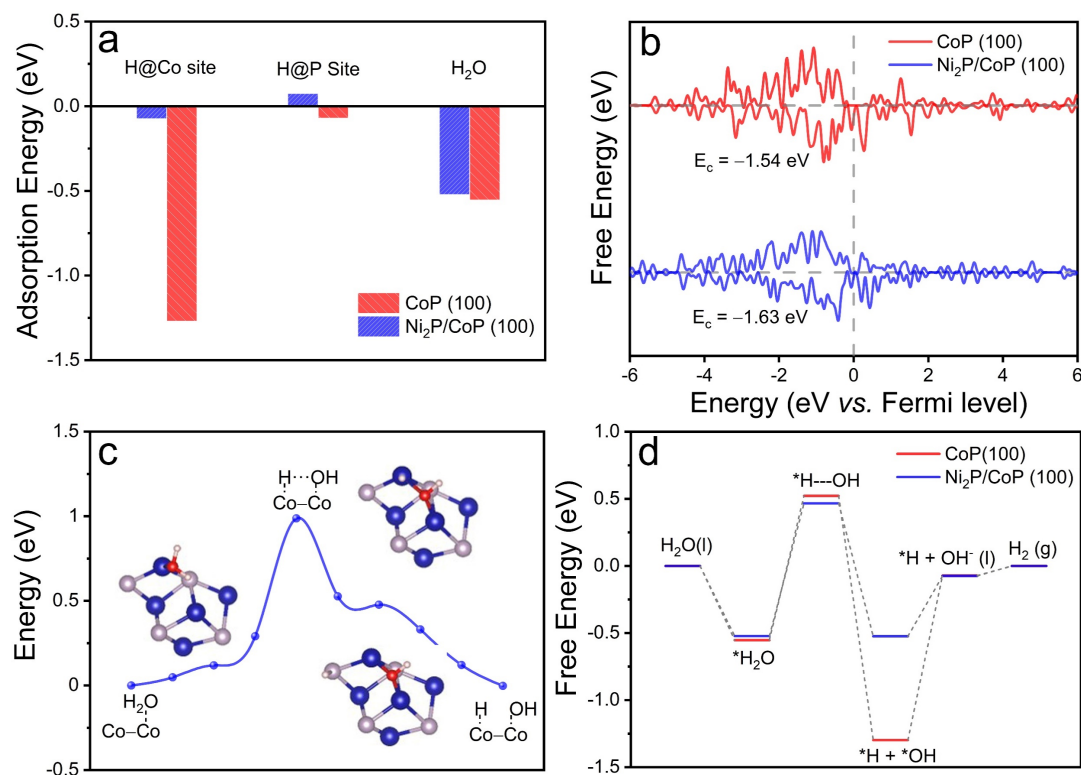

Figure 6. (a) Adsorption energy of proton over the surface of Ni_2P/CoP (100) and CoP

(100). (b) Projected density of states and d-band center of Co $3d$ for Ni_2P/CoP (100)

and CoP (100). (c) Reaction pathway of water dissociation over the surface of Ni_2P/CoP

(100) with corresponding structure of transition state. (d) Free energy diagram of

hydrogen evolution over the surface of Ni_2P/CoP (100) and CoP (100).

2.3. Density functional theory

Density functional theory (DFT) based first-principles calculations were performed to

reveal the reaction mechanism of hydrogen evolution over the surface of nickel foam

supported Ni_2P/CoP catalysts. To understand the active sites for the hybrid Ni_2P/CoP,

different Ni and Co species were synthesized, as shown in **Figure S19**. When only

Ni(OH)$_2$ or Co(OH)$_2$ precursor was prepared on the carbon paper, it shows green or pink color in **Figure S19a** and **Figure S19b**. Then Ni(OH)$_2$/ Co(OH)$_2$ precursors were prepared on carbon papers (**Figure S19c**) and Ni foam (**Figure S19d**) with both Ni(NO$_3$)$_2$ and Co(NO$_3$)$_2$ are used in synthesis. The two samples show the dark green color, which represent the robust hybridization of Ni(OH)$_2$ and Co(OH)$_2$ on the surface. While in our work, only Co(NO$_3$)$_2$ was used and the sample shows the pink color on the top surface, which represent the Co(OH)$_2$ on the top layer in **Figure S19e**. Ni comes from the substrate, thus Ni(OH)$_2$ takes a large amount in the bottom layer, then the hybrid structure of Ni(OH)$_2$/Co(OH)$_2$ in the middle layer. After phosphorating process, CoP will be formed on the top layer as shown in **Figure S19f.** Thus, two models were initially established, one was a CoP (100) surface and the other was a Ni$_2$P/CoP (100) surface (**Figure S19g**). The CoP was placed on top of Ni$_2$P. The charge density difference of CoP/Ni$_2$P model with an isosurface of 0.01 e bohr^{-3} was shown in **Figure S20**. Yellow and blue region indicate accumulation and reduction of electron. According to Bader charge analysis, 0.19 electron transfer from CoP to Ni$_2$P layer. The yellow region presents the binding between Co in CoP and P in Ni$_2$P.

We then calculated the adsorption energy of the proton over the surface of these two models (**Figure 6a**). For each model, two typical active sites, Co site and P site, were considered. The adsorption geometries of the proton are provided in **Figure S21**. For both models, adsorption energy on Co sites is more negative than P sites, which implies that Co sites are more advantageous for associative adsorption of hydrogen. The adsorption energy at Co site is too strong for the CoP (100) model, whereas the

Ni$_2$P/CoP (100) model is more favorable for hydrogen desorption with the smaller adsorption energy. The projected density of states (PDOS) of Co 3d for both two models (**Figure 6b**) was calculated. From the PDOS, the d-band center (E$_c$) of Co 3d can be obtained, which is an effective descriptor of the adsorption strength. The E$_c$ for Ni$_2$P/CoP (100) (–1.63 eV) is further away from the Fermi level than CoP (100) (–1.54 eV), in accordance with previously calculated adsorption energies. The water dissociation reaction pathway was then calculated for the Ni$_2$P/CoP (100) model (**Figure 6c**) and CoP (100) model (**Figure S22**) by using the nudged elastic band method. Co is considered as more favorable active site for water dissociation. The activation energy for the water dissociation reaction is 0.98 eV and 1.08 eV for Ni$_2$P/CoP (100) and CoP (100) model, respectively. Finally, the free energy diagram for the HER pathway was calculated (**Figure 6d**) to elucidate the relationship between the composition and the activity of the metal phosphides. The activity follows the order of Ni$_2$P/CoP (100) > CoP (100). This result is consistent with the weakened adsorption of hydrogen, benefiting for the associative desorption of hydrogen molecules, and the lower activation energy of the water dissociation reaction, which is the rate-determining step of HER in alkaline and neutral media. DFT calculations confirm the electronic states at the hybrid Ni$_2$P/CoP interface are altered to reduce the adsorption strength of hydrogen, facilitating the charge transfer kinetics and enhancing the HER performance, which is superior to the mono CoP electrocatalysts.

2.4. HER in domestic wastewater

Besides evaluating HER performance in standard neutral and alkaline media in the lab,

developing the practical application by generating hydrogen from the waste aqueous media from daily life is significant for sustainable energy production. Normally, domestic wastewater, including dishwashing, handwashing and laundry water, is just poured into the sewer without further use. Here, we choose the dishwashing wastewater as the electrolyte without adding additional chemical modifiers. The as-prepared Ni_2P/CoP was used as the working electrode, Ag/AgCl and graphite were used as reference and counter electrodes, respectively. The dishwashing liquid was purchased at a local retail outlet, which include anionic and non-ionic surfactants, benzisothiazolinone, phenoxyethanol, perfumes and limonene. The dishwashing wastewater was acquired after washing a dish, which illustrated an alkaline property (pH 9.03). The whole electrocatalytic device is presented in **Figure 7a**. The chemicals in the waste water will have an effect on the triple phase boundaries of gas/solid/liquid. Then the porous structure was compared with commercial noble metal electrocatalysts on the traditional carbon paper. The contact angle was acquired on carbon paper-Pt/C and Ni foam-Ni_2P/CoP, as shown in **Figure 7b**. The contact angle between waste water and Ni_2P/CoP was 52.9°, which was much smaller than that of Pt/C (93.8°). With more hydrophilic surfaces, Ni_2P/CoP had better performance than Pt/C in domestic waste water. At a current density of -10 mA cm^{-2}, the overpotential of Pt/C and Ni_2P/CoP-40 are 408 mV and 315 mV, respectively, as shown in **Figure 7c**. The huge difference indicates the slow reaction kinetic of Pt/C in this system. The Pt/C shows better HER performance in 1M PBS and 1M KOH, but not in the dishwashing wastewater. The Tafel slope of Pt/C and Ni_2P/CoP-40 are 463 mV dec^{-1} and 144 mV dec^{-1}, respectively,

as shown in **Figure 7d.** The huge difference between the Tafel slopes indicates the differences in rate-limiting steps for hydrogen generation. The constant current density of -10 mA cm^{-2} is maintained for 20 hours and the overpotential decreases from 329 mV to 291 mV, as shown in **Figure 7e**. The working electrode with hydrogen bubbles can be observed in the insert picture. The time-dependent hydrogen production was shown in **Figure 7f**. As for one hour test under the constant current density of -100 mA cm^{-2}, the hydrogen production was stable, which showed the efficiency of 95.1%.
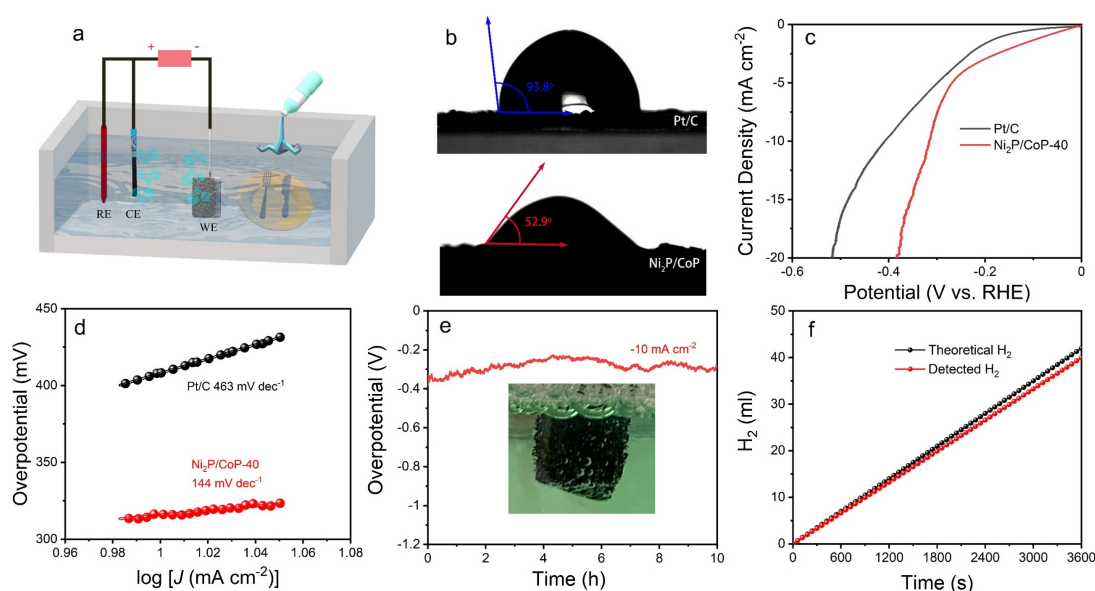

Figure 7. HER in dishwashing wastewater. (a) Graphic display of HER device with dishwashing wastewater. (b) Surface contact angle between electrocatalysts and waste water. (c) LSV curves and (d) Tafel plots of Pt/C and Ni$_2$P/CoP-40 in wastewater. (e) Chronopotentiometry measurements at a constant current of -10 mA cm^{-2}. Inset shows the working electrode with continuous H$_2$ release. (f) Time-dependent hydrogen production in waste water at a constant current of -100 mA cm^{-2}.

3. Conclusion

In summary, a facile method to fabricate a binder-free and non-noble metal

electrocatalyst of hybrid Ni_2P/CoP nanosheets on Ni foams is presented. The large specific surface area and porous structure affords a large number of active sites for HER, indicating an overpotential of 65.2 mV and 87.8 mV at a current density of -10 mA cm^{-2} in neutral and alkaline media, respectively. Both experimental and theoretical results illustrate the synergistic effect of hybrid Ni_2P/CoP in accelerating the electrochemical reaction and charge transfer kinetics, showing better or competitive HER performance among the state-of-the-art electrocatalysts. The robust interaction of self-standing electrocatalyst ensures the remarkable durability. Dishwashing wastewater was applied as the electrolyte to produce hydrogen directly. The Ni_2P/CoP nanosheets delivers an overpotential of 315 mV to reach the current density of -10 mA cm^{-2} and also presents high stability over 20h to continuously produce hydrogen from dishwashing wastewater. Our findings provide a facile way to fabricate an effective self-standing electrode and investigate its mechanism and practical applications for hydrogen production.

4. Experimental Section

Materials: Cobalt nitrate hexahydrate ($Co(NO_3)_2 \cdot 6H_2O$) and Nichol nitrate hexahydrate ($Ni(NO_3)_2 \cdot 6H_2O$) were purchased from Alfa Aesar (UK) Co., Ltd. Sodium hypophosphite monohydrate ($NaH_2PO_2 \cdot H_2O$) was purchased from Sigma-Aldrich (UK) Co., Ltd. Fairy^{TM} dishwashing liquid was purchased from local commercial outlets. Ni foam was purchased from Guangjiayuan Company. The type of carbon paper is Toray TGP-H-060.

Preparation of Carbon-$Ni(OH)_2$ and Carbon-$Co(OH)_2$ precursor: Commercial carbon paper was immersed in the 0.1M $Ni(NO_3)_2$ or 0.1M $Co(NO_3)_2$ solution for the

electrodeposition with 0.29 g of Ni(NO$_3$)$_2$·6H$_2$O or 0.292 g of Co(NO$_3$)$_2$·6H$_2$O in 100 mL of deionized water (DI) water. A Pt foil and an Ag/AgCl electrode (kept in 3M KCl solution) were used as the counter and reference electrodes, respectively. The electrodeposition process was performed under a constant current density of -10 mA cm^{-2} for 40 mins controlled by a Gamry interface 1000 potentiostat. The as-prepared electrode was dried in a vacuum oven under 60 °C overnight.

Preparation of Ni foam-Ni(OH)$_2$/Co(OH)$_2$ precursor: In a typical experimental procedure, 0.292 g of Co(NO$_3$)$_2$·6H$_2$O was added in 100 mL of DI water as the electrolyte. Commercial Ni foam was immersed in the Co(NO$_3$)$_2$ solution for the electrodeposition. The Ni foam was first put in 0.5 M hydrochloric acid solution for 10 min under ultrasonication to remove possible surface oxide layers. A Pt foil and an Ag/AgCl (kept in 3M KCl solution) were used as the counter and reference electrodes respectively. The whole electrodeposition process was under the constant current density at -10 mA cm^{-2} for 10 ~ 40 mins using a Gamry interface 1000 potentiostat. The as-prepared sample was stored in a vacuum oven at 60 °C overnight.

Preparation of carbon-Ni$_2$P, carbon-CoP, Ni foam-Ni$_2$P/CoP nanosheets: The carbon-Ni(OH)$_2$, carbon-Co(OH)$_2$ and Ni foam-Ni(OH)$_2$/Co(OH)$_2$ precursor were put into a tube furnace and heated at 350 °C with a heating rate of 5 °C min^{-1} under N$_2$ atmosphere. At the same time, 500 mg of NaH$_2$PO$_2$·H$_2$O was put into the furnace to heat for one hour under N$_2$ atmosphere. The waste gas was absorbed by sodium hypochlorite solution. The as-prepared electrode was taken out when it cooled down to room temperature. Finally, the sample was put into 0.5 M H$_2$SO$_4$ solution for 10 mins,

rinsed with DI water and put into the vacuum oven at 60 °C overnight. According to the different electrodeposition times, the as-prepared electrocatalysts were marked as CoP-40, Ni_2P/CoP-10, Ni_2P/CoP-20, Ni_2P/CoP-30 and Ni_2P/CoP-40.

Preparation of Pt/C electrode: In a typical preparation process, 10 mg commercial 20% Pt/C powder was dispersed in solution with 400 μl DI water, 100 μl ethanol and 20 μl Nafion solution, then 260 μl of the mixed solution was dropped on 1 cm^{-2} of carbon paper to fabricate the Pt/C electrodes.

Preparation of TEM sample: The Ni_2P/CoP nanosheets were scratched from Ni foam-Ni_2P/CoP from the surface. Then 1 mg of Ni_2P/CoP nanosheets were dissolve in the 200 μL methanol and put in ultrasonication for 40 mins.

Weight of deposited catalyst: The deposited catalyst was scratched from the Ni foam and weighted, at the same time, magnet was used to remove the impurity of Ni scraps. The average catalyst weights for Ni_2P/CoP-10, Ni_2P/CoP-20, Ni_2P/CoP-30 and Ni_2P/CoP-40 are 2.5 mg, 3.0 mg, 4.1 mg and 5.5 mg on 1 cm^2 Ni foam, respectively. The diagram is listed in **Figure S23**.

Calibration of Ag/AgCl electrode: A new Ag/AgCl electrode was used as reference electrode and the tested Ag/AgCl electrode was used as working electrode (all kept in 3M KCl), the open circuit voltage was examined between these two electrodes in 3M KCl, as shown in **Figure S24**. The potential margin was stable near -1 mV, which confirmed the reliability of tested Ag/AgCl electrode.

Computational Method: Density functional theory (DFT) based calculations were performed on the platform of the Vienna *ab initio* simulation package (VASP) with the

basis generated by projector augmented waves (PAW).[60] The function of Perdew, Burke and Ernzerhof (PBE)[61] was used for the description of the exchange and correlation potential. Monkhorst-Pack[62] based 3×3×1 k points were sampled in the reciprocal zone. The criteria of convergence were set to $1×10^{-5}$ eV and 0.02 eV/Å for electronic and ionic steps, respectively. The model of Ni_2P/CoP (100) surface was built *via* replacing the Co atoms of two lower layers in CoP (100) model by Ni atoms (**Figure S16**). The model contains a vacuum layer of 15 Å for avoiding the interaction between periodic images. Free energy diagrams of HER were estimated by the method referred by previous research.[63] Generally, we assume the reaction pathway of hydrogen evolution in alkaline media as:

* + $H_2O(l)$ = *H + *OH

*H + *OH + e^- = * + ½ $H_2(g)$ + OH^-
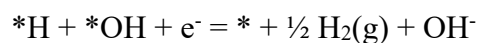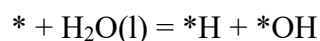
The free energy was calculated by the equation $\Delta G = \Delta E + \Delta ZPE - T\Delta S$, where the adsorption energy can be calculated as $\Delta E = E(slab) + ½E(H^+) – E(slab+H)$. The energy of H^+ and OH^- can be calculated by the equation: $G(H^+) = G(H_2O) – (1/2G(H_2) – RTln10 × pH)$, $G(OH^-) = G(H_2O) – G(H^+)$, in which R is the ideal gas constant, T is the temperature in Kelvin and pH is assumed to be 14.

The nudged elastic band (NEB) method was used for the estimation of the activation energy water dissociation reaction. The occupied *d*-band center (E_c) was calculated using equation: $E_c = \frac{\int_{-\infty}^{E_f} E\rho_d(E)dE}{\int_{-\infty}^{E_f} \rho_d(E)dE}$, where ρ_d is the PDOS of the *d*-band of Co atoms and E_f is the Fermi level.

Characterization: X-ray diffraction (XRD) patterns were obtained by a STOE

SEIFERT diffractometer with a detected angular range of $2° < 2\theta < 40°$ with a Mo X-ray radiation source. The surface morphology and elemental dispersion of the as-prepared precursors and samples were characterized by scanning electron microscope (SEM, Carl Zeiss EVO MA10) and transmission electron microscopy (TEM JEOL and JEM-2100). The chemical states of different elements were evaluated by X-ray photoelectron spectroscopy (XPS, Thermo scientific K-alpha photoelectron spectrometer) analysis. Date analysis of XPS results was processed by Casa XPS with the calibration of C 1s main peak at 285 eV. The NEXAFS experiment were performed at B07-B beamline of Diamond Light Source (UK) during a commissioning beamtime. NEXAFS measurements of Co L-edge, Ni L-edge and O K-edge were accomplished in total electron yield (TEY) mode in the ES-2 end station for Ambient Pressure NEXAFS. The catalysts powder and reference standard materials were dispersed on Indium film by pressing, which ensured good conductivity and prevented sample contamination. The samples were illuminated by incident beam sourced from a bending magnet and plane grating monochromator (PGM) with a spot size of approx. 200 μm × 200 μm. The pressure in the specimen chamber is controlled at 1×10^{-7} mbar. For each sample at each absorption edge, 3 repetitions of NEXAFS spectrum were collected and merged to improve the signal-to-noise ratio. The hydrogen production was characterized by Advance Optima AO2000 series continuous gas analyzers.

Electrochemical Performance: In the electrochemical experiment, measurements of as-prepared self-standing electrodes were conducted in a three-electrode cell. 1M KOH and 1M PBS solution was used as the electrolyte. The dishwashing wastewater

was prepared with a mixture of 5 mL Fairy^{TM} liquid and 100 mL tap water. The counter electrode was a graphite rod. Additionally, an Ag/AgCl electrode (kept in 3M KCl) was used as a reference electrode. The as-prepared Ni foam-Ni$_2$P/CoP was used as the working electrode. The surface area of the working electrode is about 1 cm^2, which is immersed in the electrolyte. The cyclic voltammetry (CV) and linear sweep voltammetry (LSV) measurements were carried out by a Gamry interface 1000 potentiostat. All potentials were measured based on an Ag/AgCl electrode and were converted to the reversible hydrogen electrode into the potential (RHE) according to the equation $E_{RHE} = E_{Ag/AgCl} + 0.197 + 0.059pH$. Tafel slopes were determined by fitting the linear regions of the Tafel plots according to the Tafel equation ($\eta = b \log(j) + a$) by replotting the polarization curves. Durability tests were evaluated by chronoamperometry measurement. Electrochemical impedance spectroscopy (EIS) was performed with frequencies from 0.1 to 100,000 Hz with an amplitude of 10 mV. All LSV measurements were calculated with full iR compensation.

Supporting Information

Additional characterization including XRD, SEM, XPS, DFT models and CV curves are provided.

Acknowledgments

Conflict of Interest

The authors declare no conflict of interest.

Reference

[1]   D. Kong, J. J. Cha, H. Wang, H. R. Lee, Y. Cui, *Energy Environ. Sci.* **2013**, *6*, 3553.

[2]   J. Mahmood, F. Li, S.-M. Jung, M. S. Okyay, I. Ahmad, S.-J. Kim, N. Park, H. Y. Jeong, J.-B. Baek, *Nat. Nanotech.* **2017**, *12*, 441.

[3]   J. Kibsgaard, T. F. Jaramillo, *Angew. Chem. Int. Ed.* **2014**, *53*, 14433.

[4]   Y. Li, H. Wang, L. Xie, Y. Liang, G. Hong, H. Dai, *J. Am. Chem. Soc.* **2011**, *133*, 7296.

[5]   J. Wang, W. Cui, Q. Liu, Z. Xing, A. M. Asiri, X. Sun, *Adv. Mater.* **2016**, *28*, 215.

[6]   Y. Tan, H. Wang, P. Liu, Y. Shen, C. Cheng, A. Hirata, T. Fujita, Z. Tang, M. Chen, *Energy Environ. Sci.* **2016**, *9*, 2257.

[7]   I. Roger, M. A. Shipman, M. D. Symes, *Nat. Rev. Chem.* **2017**, *1*, 0003.

[8]   S. Anantharaj, S. R. Ede, K. Karthick, S. Sam Sankar, K. Sangeetha, P. E. Karthik, S. Kundu, *Energy Environ. Sci.* **2018**, *11*, 744.

[9]   Y. Wu, F. Li, W. Chen, Q. Xiang, Y. Ma, H. Zhu, P. Tao, C. Song, W. Shang, T. Deng, J. Wu, *Adv. Mater.* **2018**, *30*, 1803151.

[10]   J. Zhang, L. Dai, *Angew. Chem. Int. Ed.* **2016**, *55*, 13296.

[11]   P. Hou, D. Li, N. Yang, J. Wan, C. Zhang, X. Zhang, H. Jiang, Q. Zhang, L. Gu, D. Wang, *Angew. Chem. Int. Ed.* **2021**, *60*, 6926.

[12]   N. Cheng, S. Stambula, D. Wang, M. N. Banis, J. Liu, A. Riese, B. Xiao, R. Li, T.-K. Sham, L.-M. Liu, G. A. Botton, X. Sun, *Nat. Commun.* **2016**, *7*, 13638.

[13]   H. Yin, S. Zhao, K. Zhao, A. Muqsit, H. Tang, L. Chang, H. Zhao, Y. Gao, Z. Tang, *Nat. Commun.* **2015**, *6*, 6430.

[14]   J. Zhang, Y. Zhao, X. Guo, C. Chen, C.-L. Dong, R.-S. Liu, C.-P. Han, Y. Li, Y. Gogotsi, G. Wang, *Nat. Catal.* **2018**, *1*, 985.

[15]   H. Zhang, P. An, W. Zhou, B. Y. Guan, P. Zhang, J. Dong, X. W. Lou, *Sci. Adv.* **2018**, *4*, eaao6657.

[16]   Y. Tan, R. Xie, S. Zhao, X. Lu, L. Liu, F. Zhao, C. Li, H. Jiang, G. Chai, D. J. L. Brett, P. R. Shearing, G. He, I. P. Parkin, *Adv. Funct. Mater.* **2021**, *31*, 2105579.

[17]   M. Ledendecker, S. Krick Calderón, C. Papp, H.-P. Steinrück, M. Antonietti, M. Shalom, *Angew. Chem. Int. Ed.* **2015**, *54*, 12361.

[18]   H. Wang, H.-W. Lee, Y. Deng, Z. Lu, P.-C. Hsu, Y. Liu, D. Lin, Y. Cui, *Nat. Commun.* **2015**, *6*, 7261.

[19]   Y. Jin, H. Wang, J. Li, X. Yue, Y. Han, P. K. Shen, Y. Cui, *Adv. Mater.* **2016**, *28*, 3785.

[20]   K. Hu, M. Wu, S. Hinokuma, T. Ohto, M. Wakisaka, J.-i. Fujita, Y. Ito, *J. Mater. Chem. A* **2019**, *7*, 2156.

[21]   M. A. R. Anjum, M. S. Okyay, M. Kim, M. H. Lee, N. Park, J. S. Lee, *Nano Energy* **2018**, *53*, 286.

[22]   L. Huang, D. Chen, G. Luo, Y.-R. Lu, C. Chen, Y. Zou, C.-L. Dong, Y. Li, S. Wang, *Adv. Mater.* **2019**, *31*, 1901439.

[23]   P. W. Menezes, C. Panda, S. Garai, C. Walter, A. Guiet, M. Driess, *Angew. Chem. Int. Ed.* **2018**, *57*, 15237.

[24]   S. H. Yu, W. Chen, H. Wang, H. Pan, D. H. C. Chua, *Nano Energy* **2019**, *55*, 193.

[25]   S. Zhao, J. Berry-Gair, W. Li, G. Guan, M. Yang, J. Li, F. Lai, F. Corà, K. Holt, D. J. L. Brett, G. He, I. P. Parkin, *Adv. Sci.* **2020**, *7*, 1903674.

[26]   Z. Cao, T. Zhou, X. Ma, Y. Shen, Q. Deng, W. Zhang, Y. Zhao, *ACS Sustain. Chem. Eng.* **2020**, *8*, 11007.

[27]   A. Kumar, J. Hong, Y. Yun, H. Jung, K.-S. Lee, J. W. Han, S.-J. Song, *Int. J. Hydrogen Energ.* **2021**, *46*, 30762.

[28]   I. Oh, J.-S. Youn, H. Kang, K. Manavalan, S.-C. Jung, Y.-K. Park, K.-J. Jeon, *Carbon* **2020**, *161*, 665.

[29]   X. Yang, A.-Y. Lu, Y. Zhu, M. N. Hedhili, S. Min, K.-W. Huang, Y. Han, L.-J. Li, *Nano Energy* **2015**, *15*, 634.

[30]   E. J. Popczun, J. R. McKone, C. G. Read, A. J. Biacchi, A. M. Wiltrout, N. S. Lewis, R. E. Schaak, *J. Am. Chem. Soc.* **2013**, *135*, 9267.

[31]   A. B. Laursen, K. R. Patraju, M. J. Whitaker, M. Retuerto, T. Sarkar, N. Yao, K. V. Ramanujachary, M. Greenblatt, G. C. Dismukes, *Energy Environ. Sci.* **2015**, *8*, 1027.

[32]   J. Xiao, Z. Zhang, Y. Zhang, Q. Lv, F. Jing, K. Chi, S. Wang, *Nano Energy* **2018**, *51*, 223.

[33]   P. Jiang, Q. Liu, X. Sun, *Nanoscale* **2014**, *6*, 13440.

[34]   T. Liu, P. Li, N. Yao, G. Cheng, S. Chen, W. Luo, Y. Yin, *Angew. Chem. Int. Ed.* **2019**, *58*, 4679.

[35]   S. Anantharaj, S. R. Ede, K. Sakthikumar, K. Karthick, S. Mishra, S. Kundu, *ACS Catal.* **2016**, *6*, 8069.

[36]   L. Wu, L. Yu, F. Zhang, B. McElhenny, D. Luo, A. Karim, S. Chen, Z. Ren, *Adv. Funct. Mater.* **2021**, *31*, 2006484.

[37]   Z. Wang, S. Wang, L. Ma, Y. Guo, J. Sun, N. Zhang, R. Jiang, *Small* **2021**, *17*, 2006770.

[38]   S. S. Sankar, A. Rathishkumar, K. Geetha, S. Kundu, *Int. J. Hydrogen Energ.* **2021**, *46*, 10366.

[39]   L. Yu, Y. Xiao, C. Luan, J. Yang, H. Qiao, Y. Wang, X. Zhang, X. Dai, Y. Yang, H. Zhao, *ACS Appl. Mater. Interfaces* **2019**, *11*, 6890.

[40]   F. Yu, H. Zhou, Y. Huang, J. Sun, F. Qin, J. Bao, W. A. Goddard, S. Chen, Z. Ren, *Nat. Commun.* **2018**, *9*, 2551.

[41]   H. Zhang, W. Zhou, J. Dong, X. F. Lu, X. W. Lou, *Energy Environ. Sci.* **2019**, *12*, 3348.

[42]   L. Yu, J. Zhang, Y. Dang, J. He, Z. Tobin, P. Kerns, Y. Dou, Y. Jiang, Y. He, S. L. Suib, *ACS Catal.* **2019**, *9*, 6919.

[43]   R. Wu, B. Xiao, Q. Gao, Y.-R. Zheng, X.-S. Zheng, J.-F. Zhu, M.-R. Gao, S.-H. Yu, *Angew. Chem. Int. Ed.* **2018**, *57*, 15445.

[44]   Y. Feng, R. Wang, P. Dong, X. Wang, W. Feng, J. Chen, L. Cao, L. Feng, C. He, J. Huang, *ACS Appl. Mater. Interfaces* **2021**, *13*, 48949.

[45] X. Zhang, X. Yu, L. Zhang, F. Zhou, Y. Liang, R. Wang, *Adv. Funct. Mater.* **2018**, *28*, 1706523.

[46] Y. Qu, M. Shao, Y. Shao, M. Yang, J. Xu, C. T. Kwok, X. Shi, Z. Lu, H. Pan, *J. Mater. Chem. A* **2017**, *5*, 15080.

[47] Y. Zhang, Y. Liu, M. Ma, X. Ren, Z. Liu, G. Du, A. M. Asiri, X. Sun, *Chem. Commun.* **2017**, *53*, 11048.

[48] C. Guan, W. Xiao, H. Wu, X. Liu, W. Zang, H. Zhang, J. Ding, Y. P. Feng, S. J. Pennycook, J. Wang, *Nano Energy* **2018**, *48*, 73.

[49] L. Tian, X. Yan, X. Chen, *ACS Catal.* **2016**, *6*, 5441.

[50] A. M. Hibberd, H. Q. Doan, E. N. Glass, F. M. F. de Groot, C. L. Hill, T. Cuk, *J. Phys. Chem. C* **2015**, *119*, 4173.

[51] L. Zhong, M. Barreau, V. Caps, V. Papaefthimiou, M. Haevecker, D. Teschner, W. Baaziz, E. Borfecchia, L. Braglia, S. Zafeiratos, *ACS Catal.* **2021**, *11*, 5369.

[52] M. Risch, D. Shevchenko, M. F. Anderlund, S. Styring, J. Heidkamp, K. M. Lange, A. Thapper, I. Zaharieva, *Int. J. Hydrogen Energ.* **2012**, *37*, 8878.

[53] F. Massel, S. Ahmadi, M. Hahlin, Y. S. Liu, J. H. Guo, T. Edvinsson, H. Rensmo, L. C. Duda, *J. Electron. Spectrosc. Relat. Phenom.* **2018**, *224*, 3.

[54] D. K. Bora, X. Cheng, M. Kapilashrami, P. A. Glans, Y. Luo, J. H. Guo, *J. Synchrotron Radiat.* **2015**, *22*, 1450.

[55] J. Zhang, X. Wu, W.-C. Cheong, W. Chen, R. Lin, J. Li, L. Zheng, W. Yan, L. Gu, C. Chen, Q. Peng, D. Wang, Y. Li, *Nat. Commun.* **2018**, *9*, 1002.

[56] C.-S. Hsu, N.-T. Suen, Y.-Y. Hsu, H.-Y. Lin, C.-W. Tung, Y.-F. Liao, T.-S. Chan, H.-S. Sheu, S.-Y. Chen, H. M. Chen, *Phys. Chem. Chem. Phys.* **2017**, *19*, 8681.

[57] L. Soriano, M. Abbate, A. Fernández, A. R. González-Elipe, F. Sirotti, J. M. Sanz, *J. Phys. Chem. B* **1999**, *103*, 6676.

[58] Z. Wu, L. Huang, H. Liu, H. Wang, *ACS Catal.* **2019**, *9*, 2956.

[59] Y. Zhang, L. Gao, E. J. M. Hensen, J. P. Hofmann, *ACS Energy Lett.* **2018**, *3*, 1360.

[60] P. E. Blöchl, *Phys. Rev. B* **1994**, *50*, 17953.

[61] J. P. Perdew, K. Burke, M. Ernzerhof, *Phys. Rev. Lett.* **1996**, *77*, 3865.

[62] H. J. Monkhorst, J. D. Pack, *Phys. Rev. B* **1976**, *13*, 5188.

[63] J. K. Nørskov, T. Bligaard, A. Logadottir, J. R. Kitchin, J. G. Chen, S. Pandelov, U. Stimming, *J. Electrochem. Soc.* **2005**, *152*, J23.

TOC Figure

A self-standing electrocatalyst, Ni$_2$P/CoP nanosheet was presented for efficient and robust HER process in neutral and alkaline media, showing great potential for hydrogen production by re-utilizing wastewater resources.